

## NAVY PROTOTYPE OPTICAL INTERFEROMETER IMAGING OF LINE EMISSION REGIONS OF $\beta$ LYRAE USING DIFFERENTIAL PHASE REFERENCING

H. R. SCHMITT<sup>1,2</sup>, T. A. PAULS<sup>1</sup>, C. TYCNER<sup>3</sup>, J. T. ARMSTRONG<sup>1</sup>, R. T. ZAVALA<sup>4</sup>, J. A. BENSON<sup>4</sup>, G. C. GILBREATH<sup>5</sup>,  
R. B. HINDSLEY<sup>1</sup>, D. J. HUTTER<sup>4</sup>, K. J. JOHNSTON<sup>6</sup>, A. M. JORGENSEN<sup>7</sup>, AND D. MOZURKEWICH<sup>8</sup>

<sup>1</sup> Naval Research Laboratory, Remote Sensing Division, Code 7215, 4555 Overlook Ave. SW, Washington, DC 20375, USA

<sup>2</sup> Interferometrics, Inc, 13454 Sunrise Valley Drive, Suite 240, Herndon, VA 20171, USA; [hschmitt@ccs.nrl.navy.mil](mailto:hschmitt@ccs.nrl.navy.mil)

<sup>3</sup> Department of Physics, Central Michigan University, Mt. Pleasant, MI 48859, USA

<sup>4</sup> U.S. Naval Observatory, Flagstaff Station, 10391 West Naval Observatory Road, Flagstaff, AZ 86001, USA

<sup>5</sup> Naval Research Laboratory, Free Space Photonics Communications Office, Code 5505, 4555 Overlook Ave. SW, Washington, DC 20375, USA

<sup>6</sup> US Naval Observatory, 3450 Massachusetts Avenue NW, Washington, DC 20392, USA

<sup>7</sup> New Mexico Institute of Mining and Technology, 801 Leroy Place, Socorro, NM 87801, USA

<sup>8</sup> Seabrook Engineering, 9310 Dabarry Road, Seabrook, MD 20706, USA

Received 2008 January 30; accepted 2008 October 1; published 2009 January 28

### ABSTRACT

We present the results of an experiment to image the interacting binary star  $\beta$  Lyrae with data from the Navy Prototype Optical Interferometer using a differential phase technique to correct for the effects of the instrument and atmosphere on the interferometer phases. We take advantage of the fact that the visual primary of  $\beta$  Lyrae and the visibility calibrator we used are both nearly unresolved and nearly centrally symmetric, and consequently have interferometric phases near zero. We used this property to correct for the effects of the instrument and atmosphere on the phases of  $\beta$  Lyrae and to obtain differential phases in the channel containing the  $H\alpha$  emission line. Combining the  $H\alpha$ -channel phases with information about the line strength, we recovered complex visibilities and imaged the  $H\alpha$  emission using standard radio interferometry methods. Our images show the position of the  $H\alpha$ -emitting regions relative to the continuum photocenter as a function of orbital phase, indicating a major axis line of nodes along  $\Omega = 249^\circ \pm 4^\circ$ . The orbit is smaller than previously predicted, a discrepancy that can be alleviated if we assume that the system is at a larger distance, or if the stellar continuum contribution to the  $H\alpha$  channel was underestimated. We do not detect a jet in the  $H\alpha$  images, which may be due to the limited resolution of the observations along the direction perpendicular to the orbital plane. We find that the differential phase results are consistent with those obtained from a more standard analysis using squared visibilities ( $V^2$ s) and closure phases, which also indicate an  $H\alpha$  disk radius of  $0.6 \pm 0.1$  mas, and  $\Delta V = 1.30 \pm 0.1$  and  $\Delta R = 1.20 \pm 0.1$  mag for the magnitude difference between the stars.

**Key words:** binaries: eclipsing – methods: data analysis – stars: imaging – stars: individual ( $\beta$  Lyrae) – techniques: high angular resolution – techniques: interferometric

### 1. INTRODUCTION

One of the major challenges in optical interferometry is recovering images, since fringe visibility phases are badly corrupted by the atmosphere on short timescales. A few attempts have been made to reconstruct images from the squared visibility ( $V^2$ ), an unbiased estimator of the visibility amplitude (e.g., Baldwin et al. 1996; Quirrenbach et al. 1994), but in most cases, images in optical interferometry are produced from techniques that use  $V^2$  and closure phases (e.g., Buscher 1994; Ireland et al. 2006; Monnier et al. 2007; Thiébaud 2008). These techniques have been tested and shown to reliably reconstruct images (Lawson, et al. 2006; Cotton et al. 2008). However, since a closure phase is the sum of visibility phases around a triangle of interferometer array elements, and the atmospheric turbulence effects cancel in the sum, only a fraction  $1 - 2/N$  of the phase information from an array of  $N$  elements is recovered. Therefore, a challenge for optical interferometric imaging is to recover as much of the remaining phase information as possible.

Here, we describe the technique we developed to obtain  $H\alpha$  differential phases from Navy Prototype Optical Interferometer (NPOI) observations of the interacting binary star  $\beta$  Lyrae. We were able to recover all baseline phase information for the  $H\alpha$  channel of this source. This allowed us to obtain complex visibilities, and, for the first time, to obtain  $H\alpha$  images using standard radio interferometric reconstruction techniques.

Differential phases, sometimes referred to as phase referencing (see Quirrenbach 2000, Monnier 2003 for a discussion on the subject) is an interesting and powerful technique. Here one needs multiwavelength observations obtained simultaneously and a priori knowledge about the structure of the source in a region of the observed spectrum. From that knowledge, one calculates the expected phases in that spectral region, corrects for the atmospheric and instrumental effects, and interpolates or extrapolates the corrections to the wavelengths of interest. One of the first attempts to use this technique was presented by Vakili et al. (1997, 1998), who used  $H\alpha$  and He I 667.8 nm GI2T observations of P Cygni and  $\zeta$  Tauri to detect structures in the line-emitting regions of these stars. However, they did not reconstruct images based on their measurements; their conclusions were based only on the analysis of the phases and visibilities of the stars. Another application of the differential phase technique was presented by Akeson et al. (2000), who used the Palomar Testbed Interferometer to detect variations of phase versus wavelength in data from the binary star  $\iota$  Peg. An ideal class of objects to which the differential phase technique can be applied is Be stars. These sources are composed of a B star, where the photosphere radius  $R_* \lesssim 10 R_\odot$  (corresponding to  $< 1$  mas for nearby sources) usually is unresolved by interferometric observations, surrounded by a disk of gas with a diameter of  $\sim 100 R_\odot$  (a few mas for nearby sources), which is detected in  $H\alpha$  line emission (Tycner et al. 2005).

Report Documentation Page				Form Approved OMB No. 0704-0188	
Public reporting burden for the collection of information is estimated to average 1 hour per response, including the time for reviewing instructions, searching existing data sources, gathering and maintaining the data needed, and completing and reviewing the collection of information. Send comments regarding this burden estimate or any other aspect of this collection of information, including suggestions for reducing this burden, to Washington Headquarters Services, Directorate for Information Operations and Reports, 1215 Jefferson Davis Highway, Suite 1204, Arlington VA 22202-4302. Respondents should be aware that notwithstanding any other provision of law, no person shall be subject to a penalty for failing to comply with a collection of information if it does not display a currently valid OMB control number.					
1. REPORT DATE <b>01 FEB 2009</b>		2. REPORT TYPE		3. DATES COVERED <b>00-00-2009 to 00-00-2009</b>	
4. TITLE AND SUBTITLE <b>Navy Prototype Optical Interferometer Imaging of Line Emission Regions of B Lyrae Using Differential Phase Referencing</b>				5a. CONTRACT NUMBER	
				5b. GRANT NUMBER	
				5c. PROGRAM ELEMENT NUMBER	
6. AUTHOR(S)				5d. PROJECT NUMBER	
				5e. TASK NUMBER	
				5f. WORK UNIT NUMBER	
7. PERFORMING ORGANIZATION NAME(S) AND ADDRESS(ES) <b>U.S. Naval Observatory, 3450 Massachusetts Ave, NW, Washington, DC, 20392</b>				8. PERFORMING ORGANIZATION REPORT NUMBER	
9. SPONSORING/MONITORING AGENCY NAME(S) AND ADDRESS(ES)				10. SPONSOR/MONITOR'S ACRONYM(S)	
				11. SPONSOR/MONITOR'S REPORT NUMBER(S)	
12. DISTRIBUTION/AVAILABILITY STATEMENT <b>Approved for public release; distribution unlimited</b>					
13. SUPPLEMENTARY NOTES					
14. ABSTRACT					
15. SUBJECT TERMS					
16. SECURITY CLASSIFICATION OF:			17. LIMITATION OF ABSTRACT <b>Same as Report (SAR)</b>	18. NUMBER OF PAGES <b>13</b>	19a. NAME OF RESPONSIBLE PERSON
a. REPORT <b>unclassified</b>	b. ABSTRACT <b>unclassified</b>	c. THIS PAGE <b>unclassified</b>			

**Table 1**  
Observations Log

Date	UT Range	Julian Date	No. of Scans	Baselines	Hour Angle	Orbital Phase
2005 May 09	9.63...11.90	3499.95833	5	E6-AC, AW-E6, AW-AC, AE-AC, AN-AC, AE-AN	-1.50...0.79	0.47
2005 May 18	9.85...11.80	3508.95833	10	E6-AC, AW-E6, AW-AC, AE-AC	-0.67...1.28	0.17
2005 May 19	9.58...11.75	3509.95833	9	E6-AC, AW-E6, AW-AC, AE-AC, AN-AC, AE-AN	-0.89...1.29	0.24
2005 May 24	9.08...11.63	3514.95833	8	E6-AC, AW-E6, AW-AC, AE-AC, AN-AC, AE-AN	-1.10...1.48	0.63
2005 May 26	8.98...11.36	3516.95833	10	E6-AC, AW-E6, AW-AC, AE-AC, AN-AC, AE-AN	-1.04...1.34	0.78

**Notes.** Column 3 shows the Epoch of the observations (HJD-2450000) calculated for UT = 11:00 hours, roughly the middle of the observations. The maximum lengths of the baselines shown in Column 5 are E6-AC 34.3 m, AW-E6 53.3 m, AW-AC 22.2 m, AE-AC 18.9 m, AN-AC 22.9 m, and AE-AN 34.9 m. We always used AC as the reference station.

The eclipsing binary star  $\beta$  Lyrae (HD 174638, HR 7106, FK5 705) has been extensively studied since it was discovered to be an eclipsing system over 220 years ago (Goodricke & Englefield 1785). Nevertheless, it remains one of the most baffling binary systems known (see Harmanec 2002 for a comprehensive review). The current model consists of a  $\sim 3 M_{\odot}$  B6-8II star (star 2 in Harmanec's notation), which has filled its Roche lobe and is losing mass at a rate of  $2 \times 10^{-5} M_{\odot} \text{ year}^{-1}$  to a  $\sim 13 M_{\odot}$  early B star (star 1), which is completely embedded in and hidden by a thick accretion disk. This accretion disk simulates a pseudophotosphere, which appears to an observer to have a spectrum of an A5III star (for a diagram of the  $\beta$  Lyrae system we refer to Figure 8 in Linnell et al. 1998 and Figure 8 in Hoffman et al. 1998). The orbit is very nearly circular, the orbital period is a little over 12.9 days, and the period is increasing by  $19 \text{ s year}^{-1}$ . The system lies at a distance of  $270 \pm 39 \text{ pc}$ , as measured by *Hipparcos* (Perryman et al. 1997). The spectrum of  $\beta$  Lyrae contains at least six spectroscopic line components (Harmanec 2002). The three major components are (1) strong absorption lines from star 2 used to derive the radial velocity curve having an amplitude of  $370 \text{ km s}^{-1}$ , (2) "shell" absorption components seen in the hydrogen, helium, and many metallic lines, believed to arise from the accretion disk, and (3) strong lines of hydrogen and helium seen in emission, which vary with the orbital phase and time. One of the features that makes  $\beta$  Lyrae unique among contact binaries is the possibility that the strong emission lines come from a bipolar jet that has formed near the point where material streaming from star 2 interacts with the accretion disk around star 1 (Harmanec et al. 1996).

This paper is organized in the following way. In Section 2, we present the observations and reductions. In Section 3, we describe the corrections applied to the data in order to obtain differential phases and describe the results obtained for  $\beta$  Lyrae. In Section 4, we describe the imaging of the  $H\alpha$  emission of this source. In Section 5, we obtain information about the orbit of this system from the displacement of the  $H\alpha$  emission relative to the continuum photocenter. In Section 6, we compare the results obtained from the analysis of the  $H\alpha$  images with those obtained using a traditional  $V^2$  analysis, and in Section 7, we give a summary of our results.

## 2. OBSERVATIONS AND REDUCTIONS

### 2.1. Interferometry

Our observations were taken with the NPOI (Armstrong et al. 1998) on five different nights between 2005 May 9 and 2005 May 26. The observations were made with two spectrographs, simultaneously recording fringes in 16 spectral channels in the wavelength range 560–860 nm. Between one and three baselines were measured with each spectrograph. The maximum baseline

lengths ranged from 18.9 to 53.3 m. In Table 1, we present a log of the observations, including the number of scans observed each night, the baselines used, and the range of hour angles covered by the observations. Figure 1 presents the  $(u, v)$ -plane coverage achieved by the observations on each night. For reference, this figure also shows the array layout with the stations and baselines used. The observations of  $\beta$  Lyrae were interleaved with observations of a nearby calibrator star  $\gamma$  Lyrae (B9III,  $V = 3.24 \text{ mag}$ ), which has a similar spectral type and magnitude to that of  $\beta$  Lyrae. Each calibrator or source scan had a duration of 30 s.

Throughout this paper we will use orbital phases of  $\beta$  Lyrae based on the latest ephemeris of primary eclipses from Kreiner (2004).<sup>9</sup> We assumed a single orbital phase for each night, corresponding to the midpoint of the observations (Table 1). This assumption will have no effect on the final results of this paper, because our observations usually lasted for  $\sim 2 \text{ hr}$ , which corresponds to  $\sim 0.6\%$  of an orbital period. Comparing the values obtained from this ephemeris with those from Harmanec & Scholz (1993), we find that the two predictions agree at the 2% level, which is sufficient for the purposes of the analysis presented here. As a final check, we compared the predicted times of minima with visual measurements from AAVSO,<sup>10</sup> spread over a period of two months around our observations. We used only validated observations available at the AAVSO site and got an agreement better than 0.25 days between the observed and predicted minima, which corresponds to  $\sim 2\%$  of the orbital period.

The initial data reductions followed the incoherent and coherent integration methods described in Peterson et al. (2006a). In the case of the incoherent integration, we start with data that were processed to produce squared visibilities ( $V^2$ ) averaged into 1 s intervals. These data are then flagged to eliminate points with fringe tracking and pointing problems (Hummel et al. 1998, 2003a). The flagged data set is then used to bias correct the  $V^2$  data, which are then calibrated. The calibrated  $V^2$  values are later used to estimate the amplitudes of the complex visibilities.

For the coherent integration of complex visibilities, we use the technique presented by Hummel et al. (2003b; see Jorgensen et al. 2007 for a different algorithm). We treat the visibilities in each 2 ms frame (the instrumental integration time) as phasors. To determine the phase shift from one frame to the next, we compute the power spectrum of the channeled visibility as a function of delay and measure the phase difference between the peak of the fringe envelope and the nearest fringe peak. We rotate the phasors to correct for this residual phase and average the complex visibilities in 200 ms subscans, which are used

<sup>9</sup> <http://www.as.wsp.krakow.pl/ephem/LYR.HTM>

<sup>10</sup> [www.aavso.org](http://www.aavso.org)

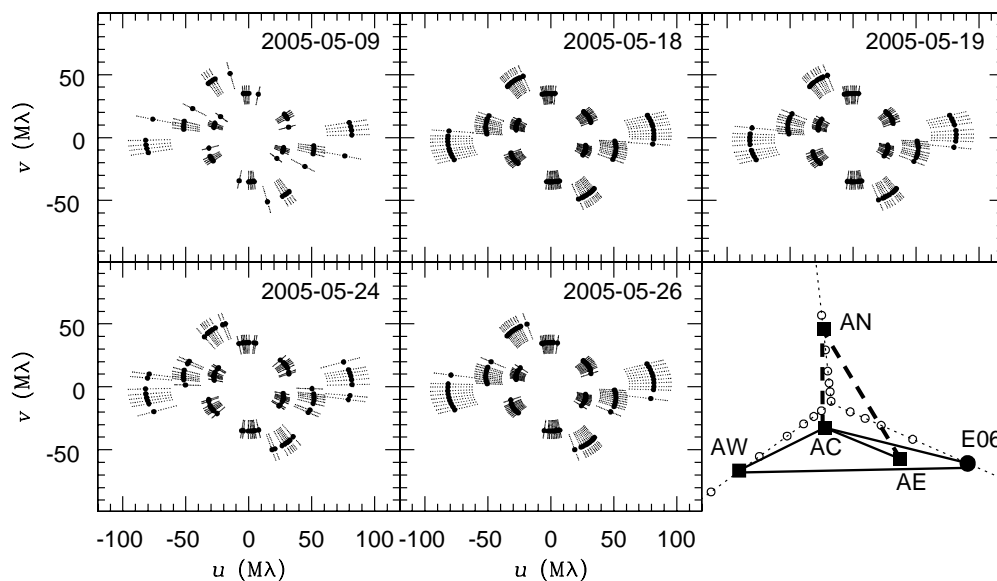


**Figure 1.**  $u - v$  coverage of the different nights. The small points show the continuum channels, while the large ones show  $H\alpha$ . The observing date is presented in the top right corner of each panel. The bottom right corner of the figure shows the array layout. The astrometric stations are shown as black squares and E06 is shown as a black dot. We also show the baselines used on all nights as solid lines and the baselines that were used only on some nights, those involving AN, as dashed lines. The maximum baseline lengths can be found in Table 1.

to determine the visibility phases. In Section 3, we describe other corrections applied to these data in order to obtain  $H\alpha$  differential phases for  $\beta$  Lyrae.

## 2.2. Spectroscopy

To estimate the strength of the  $H\alpha$  emission in the  $\beta$  Lyrae system, we have obtained a high-resolution spectrum using a fiber-fed Echelle spectrograph at the Lowell Observatory's John S. Hall telescope. The spectrum was acquired on 2005 May 19, which corresponds to the middle of our interferometric run. The spectroscopic data were processed using standard routines, developed specifically for the instrument used in the observations (Hall et al. 1994). The final reduced spectrum in the  $H\alpha$  region reaches a resolving power of 10,000 and a signal-to-noise ratio (S/N) of few hundreds (see Figure 2).

We obtain an equivalent width (EW) of  $-1.5 \pm 0.05$  nm for the  $H\alpha$  profile shown in Figure 2. Most of the uncertainty in the EW measurement is due to the uncertainty associated with continuum normalization, which is estimated to be of the order of 3%. To obtain the total emission in the  $H\alpha$  line, we also need to correct for the underlying stellar absorption line that has been filled in by the emission from the circumstellar material. We estimate the EW of the underlying absorption line using the calibration developed by Coté & Waters (1987). Using a reddening-corrected color  $(B - V)_0 = -0.05$  mag for  $\beta$  Lyrae from Dobias & Plavec (1985), we obtain an EW of 0.72 nm for the  $H\alpha$  absorption component, and therefore we estimate that the EW of the *total*  $H\alpha$  emission is  $-2.2$  nm. Considering that the NPOI  $H\alpha$  channel has a width of  $15 \pm 1$  nm and the total emission line width is  $-2.2$  nm, we derive a fractional contribution from the stellar photosphere ( $c_{\text{ent}}$ ) to the total flux in the channel of  $0.87 \pm 0.01$ .

## 3. DIFFERENTIAL PHASES

The challenge of recovering phase information from optical interferometric observations results from atmospheric and instrumental effects, changing the phase calibration on a timescale of a few milliseconds. Fringe tracking can reduce

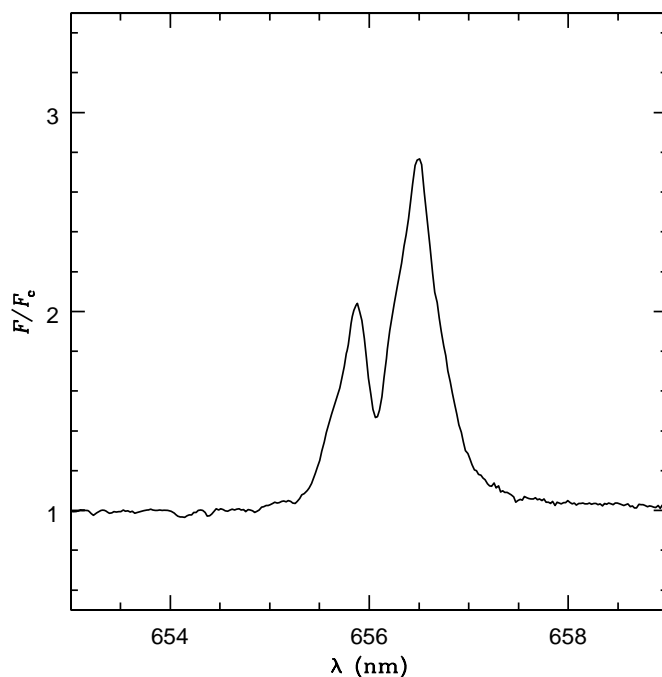


**Figure 2.** High-resolution  $H\alpha$  profile of  $\beta$  Lyrae, normalized to the mean continuum level.

these variations but not to the level needed for good imaging. Even with fringe tracking, the solution starts with (1) short exposures that freeze the fringe motion, (2) software that measures and removes these variations and, (3) a coherent integration of hundreds of milliseconds (or more) needed to increase the S/N to a level sufficient for the rest of the data processing. The result is a measurement of the real and imaginary parts of the visibility. The uncorrected phase variations during the coherent integration consist of a constant part and zero mean fluctuations. The fluctuations reduce the measured visibility amplitude but have no effect on the phase. Thus, these visibility data can be processed using closure relationships or self-calibration.

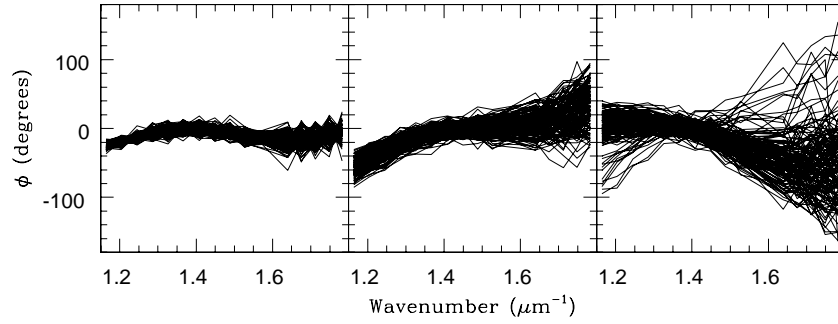


**Figure 3.** Coherently integrated phases of three scans of the calibrator  $\gamma$  Lyrae, observed on 2005 May 9 with baseline AW0–E06 at UT = 9:38 (left), 11:23 (middle), and 11:55 (right). Each line corresponds to a different 200 ms subscan.

However, with a small number of stations, there are significantly more baselines than closure phases, so a significant fraction of phase information is lost. By contrast, the differential phase technique described here provides good phase information for every baseline. The idea is to recognize that the observed phase consists of three terms, viz., the desired source phase  $\phi_0$ , and offsets caused by the atmosphere and the instrument:

$$\phi_{\text{obs}} = \phi_0 + \phi_{\text{atm}} + \phi_{\text{inst}}. \quad (1)$$

All terms have implicit wavelength dependences. The differential phase technique consists of (1) measuring  $\phi_{\text{obs}}$  at several wavelengths, (2) modeling the three right-hand side terms in Equation (1), and (3) deriving parameters of the model by fitting it to the measured  $\phi_{\text{obs}}$ . For the NPOI,  $\phi_{\text{inst}}$  is stable and can be estimated by observing calibration stars; no parameters need to be fitted. The atmospheric term,  $\phi_{\text{atm}}$ , is given by

$$\phi_{\text{atm}} = a(n-1)k + dk + \phi_c, \quad (2)$$

where  $a$  is the differential air path between two beams,  $n$  is the refractive index of air,  $k$  the wavenumber ( $2\pi/\lambda$ ),  $d$  the vacuum path difference, and  $\phi_c$  is a wavelength-independent phase offset (Jorgensen et al. 2006). Three quantities need to be fitted:  $a$ ,  $d$ , and  $\phi_c$ . Thus, with at least four spectral channels, some information about the source can be obtained for *each* baseline.

### 3.1. Instrumental and Atmospheric Corrections

The  $H\alpha$  emitting circumstellar disks of Be stars constitute one of the best cases for which one can calculate instrumental and atmospheric corrections to the visibility phases. This correction is based on observations of calibrator stars and the continuum channels of the star of interest. Since the photospheres of these stars usually do not deviate significantly from point symmetry, we can model the continuum as having zero intrinsic phase. Even in the case of rapidly rotating stars, in which the stellar image may deviate from point symmetry, the phase should vary smoothly and slowly with wavelength (Yoon et al. 2007; Peterson et al. 2006a, 2006b). The same principle applies to calibration stars. These properties allow one to use the information from the continuum channels to calculate the appropriate corrections to the phases and interpolate them over the channel containing the  $H\alpha$  line.

A first example of the instrumental and atmospheric effects on the phases of a partially resolved star is shown in Figure 3. Each panel of this figure shows a different scan of  $\gamma$  Lyrae, while the different lines in each panel represent individual 200 ms subscans. Note that the lines of the different subscans follow a similar cubic like shape as a function of wavenumber, with some

scatter. This cubic curve can be explained as an instrumental phase due to uncompensated amounts of glass along the different beams. This curve does not change significantly from scan to scan, or from night to night. A further inspection of this figure shows that, besides this cubic component, one can also see a significant variation of the phase among different subscans. These variations are due to the differential air path between the two beams, and the shape of the curve is due to the fact that  $(n-1)$  has a significant dependence on  $k^2$  (Owens 1967). One can also see in Figure 3 that the scatter is much smaller in the left panel, during the first scan of the night, increasing significantly toward later times (right), consistent with the worsening of the seeing conditions through the night.

In order to obtain differential phases of Be stars, one needs to correct the data for the two components described above. For the instrumental phases we use the values determined by averaging all the 200 ms subscans of calibrator stars observed throughout the night. Since the effects of the differential air path and vacuum delay are random and constitute an additive term to the intrinsic phases, one can reasonably assume that they should average down to zero over the course of a night. Also, since calibration stars are expected to have zero phase in the spectral range covered by our observations, by averaging the complex visibilities of the calibrators one is left only with instrumental phases, which can then be subtracted from the program star visibilities.

We demonstrate the procedure used to obtain instrumental phases in Figure 4. Here we show the phases obtained by averaging the visibilities of all 720 subscans of  $\gamma$  Lyrae observed on the same night (white line). We can also show that the other component affecting the phases of the subscans is due to differential air path between the two beams. Following the derivation presented by Armstrong et al. (1998), we expand Equation (2) into a power series around  $k_0$  and rewrite Equation (1) in the following form:

$$\phi_{\text{obs}} = \phi_0 + \phi_{\text{inst}} + c_0 + c_1k + c_2k^2. \quad (3)$$

Starting from this equation and assuming that  $\phi_0 = 0$ , one can then solve for the coefficients  $c_0$ ,  $c_1$ , and  $c_2$  for each subscan, such that the residuals produce the best fit to the atmosphere phases ( $\phi_{\text{obs}} - \phi_{\text{inst}}$ ). We show in Figure 4, as black lines, all subscans after subtracting only the atmosphere effects from the observed phases. Note that these lines follow the instrumental one. Figure 4 also shows histograms with the distribution of phases after the subtraction of atmospheric effects. These histograms show that the phases have a much lower scatter in the red part of the spectrum, where the S/N is higher. The uncertainties in the mean values of the instrumental phases



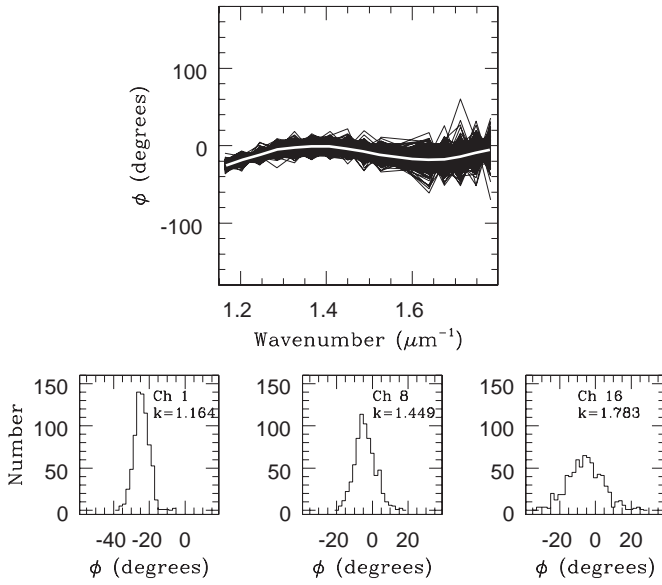


**Figure 4.** Top panel shows the comparison between the phases of individual subscans of  $\gamma$  Lyrae from Figure 3, corrected for atmospheric and vacuum delay effects but not for the instrumental phase, which are shown as a white line. The instrumental phases were obtained by averaging all subscans of this calibrator star observed in this particular night. This figure demonstrates that the average phase of  $\gamma$  Lyrae is a good estimator of the instrumental phase. The bottom panels show histograms of the distribution of the corrected phases in three different channels. The uncertainty in the mean value of the instrumental phase depends on  $N^{-1/2}$  (number of coherently integrated subscans), which in this case is 720. It grows from  $0^{\circ}17$  in channel 1 (reddest one), to  $0^{\circ}24$  in channel 8, and  $0^{\circ}42$  in channel 16 (bluest one).

depend on  $N^{-1/2}$  (number of subscans), varying from  $\sim 0^{\circ}15$  in the red to  $\sim 0^{\circ}5$  in the blue.

### 3.2. Differential Phases of $\beta$ Lyrae

The correction steps applied to the data of the program star ( $\beta$  Lyrae) to obtain the phase in the  $H\alpha$  channel are presented in Figure 5. In order to simplify the procedures and reduce the number of calculations, we take advantage of the fact that the atmospheric effects constitute a random and additive phase term, so instead of dealing with individual 200 ms subscans we can work with the average of all visibilities in a scan. The left panel of Figure 5 shows the average phases of nine scans of  $\beta$  Lyrae. In the central panel, we show the phases of the individual scans after the subtraction of the instrumental phase, shown as a dashed line in the left panel. The last step of the process is

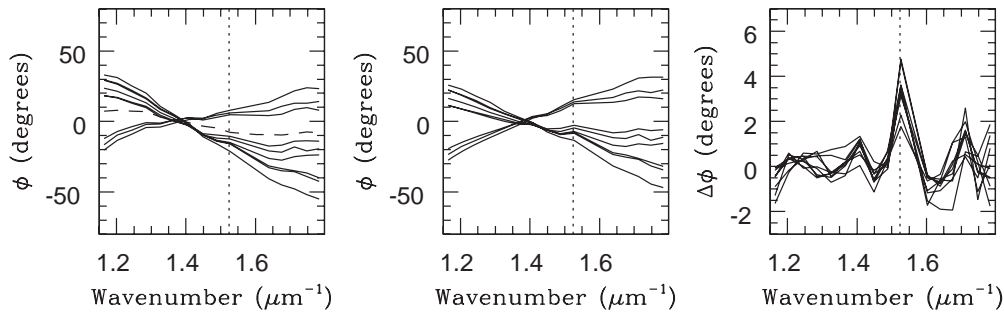


**Figure 5.** Different correction steps applied to the data of  $\beta$  Lyrae. The first panel (left) shows the average phases of each scan (solid lines) for baseline E06–AC0, obtained on 2005 May 19. The dashed line shows the instrumental phases, obtained from the calibrator stars, and the dotted vertical line shows the location of the  $H\alpha$  channel. The middle panel shows the phases obtained after subtracting the instrumental contribution. The right panel shows the differential phases obtained after subtracting a quadratic function, which was fitted to the continuum points only for each scan presented in the middle panel. The uncertainty in the phases is of the order of  $0^{\circ}3$  in the red,  $0^{\circ}5$  at  $H\alpha$ , and grows to  $1^{\circ}$  in the blue.

the correction of the atmospheric effects by fitting a quadratic function of the form of Equation (3) to the continuum channels for each average scan and subtracting the resulting function from all the channels. These results are presented in the right panel of Figure 5, where we can see that the resulting continuum phases are close to zero, while the  $H\alpha$  ones are between  $2^{\circ}$  and  $5^{\circ}$ . This range of values is due to changes in the projected baseline length over the night.

In the procedures described above, the continuum phases of  $\beta$  Lyrae were assumed to be zero. Nevertheless, one should expect to see phase variations across the spectrum.  $\beta$  Lyrae is a binary system with a maximum separation of  $\sim 1$  mas and  $\Delta m \sim 0.9$  mag, with almost no color difference between the two components (Wilson 1974; Harmanec 2002). Using Equation (8) of Mourard et al. (1992), we calculate that observing this system at maximum separation with a 50 m baseline aligned with the separation vector should show a continuum phase  $\phi_{\text{cnt}}$  of  $\sim 14^{\circ}$  at the  $H\alpha$  channel, with a slope of  $1^{\circ}$  per channel. This case corresponds to the longest baseline in our data, but most of our baselines were 34 m long or less. For a 30 m baseline,  $\phi_{\text{cnt}}$  at  $H\alpha$  is  $1^{\circ}6$  with a slope of  $0^{\circ}2$  per channel.

Although the continuum phase component varies smoothly with wavenumber and can be modeled by our atmospheric phase subtraction method, arbitrarily setting this component to zero can, in principle, influence our results. The complex visibility of the  $H\alpha$  channel results from the sum of the complex visibility of the continuum and  $H\alpha$  emission line. Setting the continuum phase to zero will change the phase of the emission line visibility by  $\phi_{\text{cnt}}$ . For baselines of 30 m or smaller this is not an important effect, given the small continuum phases. However, as shown above, in the case of our longest baseline this can change the  $H\alpha$  emission phase by as much as  $\sim 14^{\circ}$ . We discuss in Section 4 how we tested the effect of this assumption on the imaging of this source.

Figure 6 shows the differential phases of  $\beta$  Lyrae on all baselines observed on 2005 May 19. Here we see results similar to those from Figure 5, with the continuum phases around zero, and the  $H\alpha$  and  $He\text{ I}$  channels showing a differential phase. The strongest  $H\alpha$  phase is found on baselines with the longest extent along the E–W direction, with very little differential phase signals on baselines AN0–AC0 and AE0–AN0. Comparing these results with those from Mourard et al. (1992) and Harmanec et al. (1996) we get a consistent picture for this system. Based on GI2T observations, Harmanec et al. (1996) concluded that the orbit of the binary component should be roughly oriented along the east west (E–W) direction, since

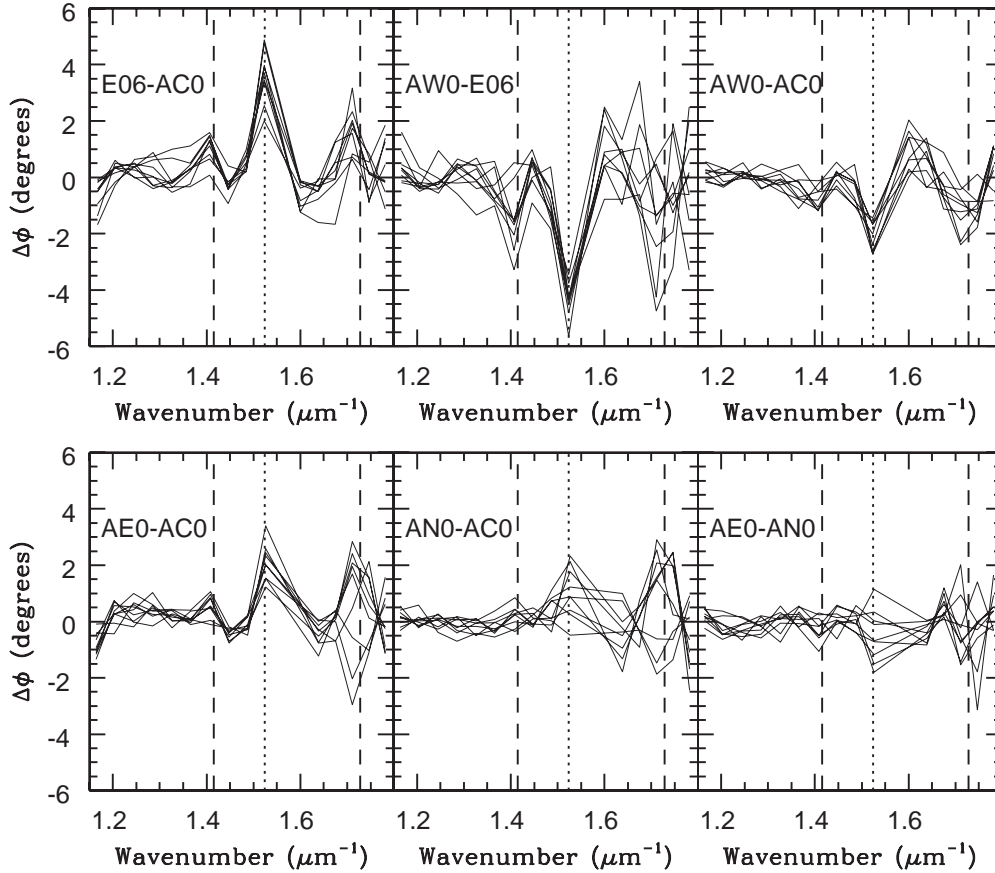


**Figure 6.** Residual phases of  $\beta$  Lyrae after correcting for the instrumental, atmospheric and vacuum differential delay effects. Each panel shows a different baseline, observed on 2005 May 19. The individual lines represent individual scan averages. The vertical dotted line indicates the wavenumber of  $H\alpha$ , while the dashed lines show the wavenumbers of the He I 706.5 nm and 587.6 nm emission lines.

their observations used an north south (N–S) baseline and did not resolve the two stars. On the other hand, their line observations detected smaller  $V^2$ s for  $H\alpha$  and He I indicating that the line-emitting region is more extended along the N–S direction. This result is consistent with the spectropolarimetric observations from (Hoffman et al. 1998), who found that  $H\alpha$ , He I 587.6 nm, and ultraviolet ( $\lambda < 360$  nm) emission are polarized along p.a.  $\sim 74^\circ$ . This result indicates that this emission is polarized by a structure perpendicular to this direction. Another result that confirms this geometry is a radio nebula along p.a.  $156^\circ \pm 4^\circ$  detected by Umana et al. (2000).

Comparing our results to those from Harmanec et al. (1996) suggests a possible contradiction, since we do not see a strong differential phase on the baselines oriented closer to the N–S direction, at least when comparing their signal to that measured on baselines oriented closer to the E–W direction. However, our observations can be explained in a way that agrees with the previous results. First, the weaker phase signal along the N–S direction can be explained in part as an effect of the baseline lengths of the two observations. Harmanec et al. (1996) used a baseline of 51 m, while for our AE0–AN0 baseline we have a longest projected length of only  $\sim 25$  m along the N–S direction. Our maximum baseline length along the E–W direction is roughly twice that, which can explain the stronger differential phase signal along this direction. Second, we interpret the differential phases as a displacement between

the  $H\alpha$  line-emitting region and the continuum photocenters. Since the binary system is expected to be oriented along the E–W direction, this would explain the stronger  $H\alpha$  differential phases on baselines aligned closer to this direction.

Further support for this interpretation is presented in Figure 7, where we show the differential phases of baseline AW0–E06 on 2005 May 19 and 2005 May 26. These observations correspond to orbital phases of 0.24 and 0.78, respectively. Here, we can see that the  $H\alpha$  phase signal changes from negative to positive between the two dates, which can be understood as the center of line emission and continuum photocenter changing orientation relative to each other.

We would also like to point out another interesting result from Figure 6, the variation of the He I differential phases near  $k \sim 1.4$  and  $1.7 \mu\text{m}^{-1}$ , in particular on baselines AE0–AC0 and AN0–AC0. One can see in this figure that the He I channel phases vary significantly from scan to scan, with the sign of the phase changing from positive to negative in a few scans. When we compare this behavior to that of the  $H\alpha$  phases, we see that  $H\alpha$  does not change sign on the same night. This result indicates that the He I emitting region has a structure different from that of the  $H\alpha$  region. This conclusion is supported by the spectropolarimetric results from Hoffman et al. (1998), who found that He I 587.6 nm and He I 706.5 nm have polarization properties different from those of  $H\alpha$  and He I 667.8 nm. This difference is due to the way these lines are excited, with the 587.6 ( $k = 1.70 \mu\text{m}^{-1}$ ) and 706.5 nm ( $k = 1.42 \mu\text{m}^{-1}$ )

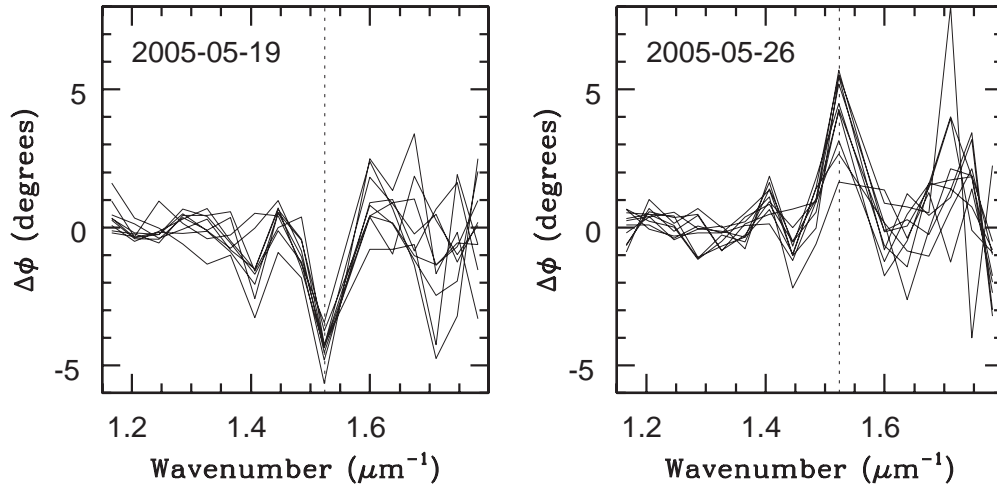


**Figure 7.** Comparison of the differential phases of the longest baseline AW0-E06 (53 m) on the nights of 2005 May 19 (left) and 2005 May 26 (right). The two nights are separated by approximately half an orbital period.

being produced in higher density regions, possibly in the inner accretion disk, consistent with the observed differences in the phases of these emission lines.

#### 4. IMAGING

The ultimate goal of our differential phase experiment is the recovery of complex visibilities of this star in order to image the H $\alpha$  and continuum emission. In order to do this we start by combining the final phase information described above with the calibrated  $V^2$ s from the incoherent integration method to calculate the corresponding complex visibilities for both continuum and line channels. Since these visibilities have been corrected for instrumental and atmospheric effects, the continuum channels can be exported into a FITS file and imaged using the usual radio interferometry techniques. However, in order to image the H $\alpha$  emission one needs to take into account the fact that most of the light in this channel originates from the continuum.

The correction for the continuum contribution to the H $\alpha$  channel is calculated using the  $c_{\text{cnt}}$  value obtained from the spectroscopic measurements. Rewriting Equation (1) of Tycner et al. (2006) in a more general form, we have the following relation for the continuum-subtracted H $\alpha$  complex visibility:

$$V_{\text{H}\alpha} = (V_{\text{obs}} - c_{\text{cnt}} V_{\text{cnt}}) / (1 - c_{\text{cnt}}). \quad (4)$$

$V_{\text{obs}}$  is the observed complex visibility in the H $\alpha$  channel, including the line and continuum components,  $V_{\text{cnt}}$  and  $V_{\text{H}\alpha}$  are the complex visibilities of the continuum and H $\alpha$  components, and  $c_{\text{cnt}} = 0.87$  is the fractional contribution from the stellar continuum to the total flux in the H $\alpha$  channel (Section 2.2). We use the averaged visibility of the two channels adjacent to H $\alpha$  to estimate  $V_{\text{cnt}}$  at the H $\alpha$  channel.

The resulting visibilities are converted into FITS files (one per night) and imaged using AIPS<sup>11</sup> (van Moorsel et al. 1996). The resulting H $\alpha$  images are presented in Figure 8. These images were created using pixel sizes of 0.5 mas and a hybrid weighting scheme. We used a combination between natural and uniform weights, with robustness index 0, which is a good compromise between resolution and sensitivity. Just for reference we show in each panel, as a white cross, the position of the continuum

photocenter, measured on continuum images restored from data observed on the same night. The position of the continuum was always in the center of the image, consistent with the fact that the continuum phases were set to  $\sim 0^\circ$  in our procedures. Note that in most cases the H $\alpha$  emission has a shape similar to that of the restoring beam, which indicates that the emission is just partially resolved, with a size comparable to that of the beam. We do not find evidence of a jet in these images, but this does not rule out the presence of one, since our lowest resolution is along the N–S direction, where the jet is expected to be found (Harmanec et al. 1996).

The most important result to be taken from Figure 8 comes from the comparison between the peaks of the H $\alpha$  and continuum emission. We can see in the different panels that these two points do not coincide, and that the displacement of the H $\alpha$  photocenter changes relative to that of the continuum as a function of orbital phase. Since the H $\alpha$  emission originates in the disk around the more massive star, while the continuum photocenter is located closer to the less massive one (Harmanec et al. 1996), we are effectively imaging the orbit of this system.

We also tested the effect introduced in the H $\alpha$  images of assuming that the continuum phase on the longest baseline is zero. To solve for this effect, we added  $14^\circ$  to the phases of both H $\alpha$  and adjacent continuum channels of the longest baseline before subtracting the continuum contribution to the H $\alpha$  channel. We did not try to apply this correction to other baselines because of the small magnitude of their continuum phases. We followed the procedure described above and obtained new images using the uncorrected short baseline H $\alpha$  visibilities and the corrected long baseline H $\alpha$  visibilities. We do not find a significant change relative to the images obtained setting the continuum phase to zero. The position of the peaks of emission changed less than  $0.4\sigma$ , indicating that setting the continuum phases to zero was a reasonable approximation in this case.

#### 5. THE ORBIT OF THE H $\alpha$ EMISSION IN $\beta$ LYRAE

Although we barely resolve the stars in this binary, our results can be used to derive some properties of the  $\beta$  Lyrae system. First, since this is an eclipsing binary, it is straightforward to determine the orientation of the system on the plane of the sky. The inclination of the orbit is  $86^\circ$  (Linnell et al. 1998; Linnell 2000) and its projection on the sky can be reasonably well approximated by a straight line. In Figure 9, we show

<sup>11</sup> [www.aips.nrao.edu](http://www.aips.nrao.edu)



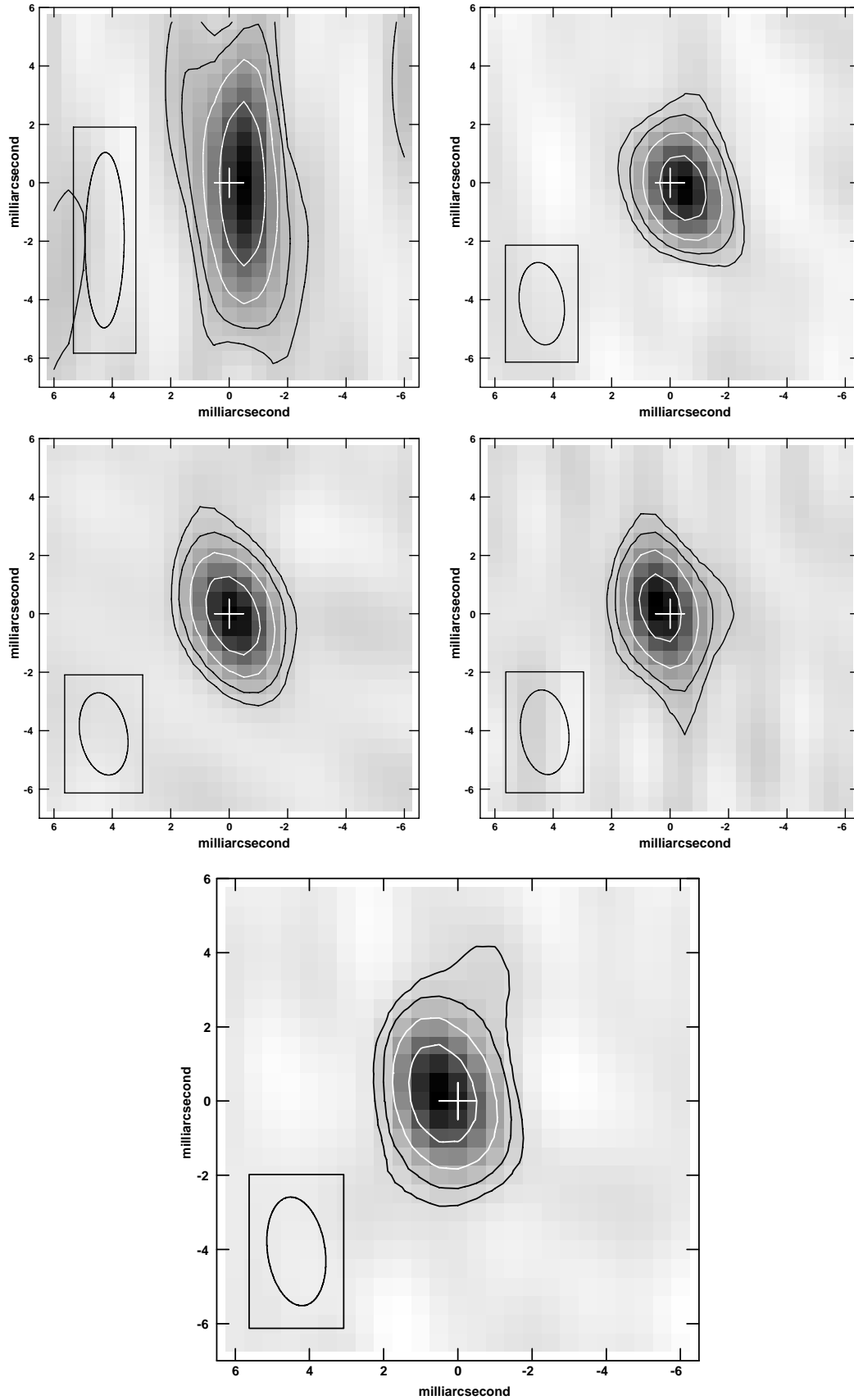


**Figure 8.** Images of the  $H\alpha$  emission from  $\beta$  Lyrae, shown as both grayscale and contours. Each of these figures corresponds to a different night, organized in order of increasing orbital phase (top left: 2005 May 18; top right: 2005 May 19; middle left: 2005 May 9; middle right: 2005 May 24; bottom left: 2005 May 26). The cross shows the position of the photocenter of the system, measured on continuum images. The lowest contour in each figure corresponds to the  $3\sigma$  noise level. The reconstructing beam is shown in the bottom left corner of each figure.

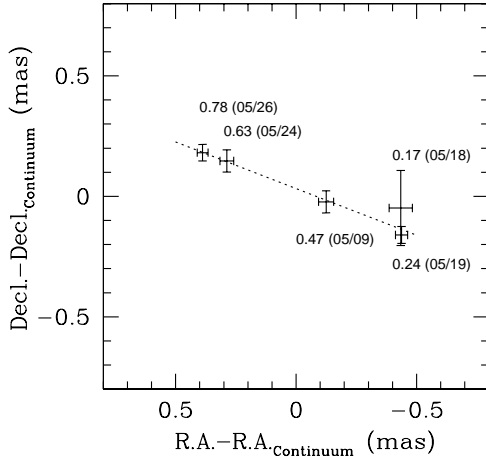


**Figure 9.** Positions of the peak of  $H\alpha$  emission relative to the continuum photocenter. For each point we show the position uncertainty, obtained by fitting a Gaussian to the image of the source. Beside each point we also indicate the orbital phase and the date of the observation. The dotted line was obtained by fitting a least-squares line to the data. Since  $\beta$  Lyrae is an eclipsing binary, this line is a good approximation for the orientation of the orbit in the plane of the sky:  $\Omega_{H\alpha} = 249^\circ$ .

the position of the  $H\alpha$  emission relative to the continuum photocenter for the five nights of data used in this paper. These positions were obtained by fitting Gaussians to the images, and the values are given in Table 2.

Figure 9 shows an initial estimate of the position angle of the line of nodes,  $\Omega_{H\alpha} = 248.8 \pm 1.7$ , from fitting a straight line to these positions. Note that the point from 2005 May 18 has a much higher uncertainty in the N–S direction, caused by the absence of the northernmost station, ANO, and the resulting loss of resolution in this direction. We fit an orbit for the positions of  $H\alpha$  emission region around the photocenter using instrumental weighting ( $1/\sigma^2$ ), holding the period, inclination, and eccentricity fixed and allowing the semimajor axis  $a_{H\alpha}$ , the line of nodes  $\Omega_{H\alpha}$ , and the time of periastron passage just preceding our observations,  $T_{H\alpha}$ , to vary. We find  $a_{H\alpha} = 0.46 \pm 0.03$  mas,  $\Omega_{H\alpha} = 249^\circ \pm 4^\circ$ , and  $T_{H\alpha} = \text{JD}2453493.77 \pm 0.23$ . Repeating this fit without the data point for 2005 May 9, when the  $H\alpha$  disk is partially hidden by star 2, does not change the results significantly (less than the half the quoted uncertainties).

The reliability of  $\Omega_{H\alpha}$  we obtain for the  $\beta$  Lyrae system can be checked by comparing with other measurements available in the literature. The radio observations presented by Umana et al. (2000) detected a jetlike nebular structure oriented along p.a. =  $156.5^\circ \pm 4^\circ$ . This nebula is perpendicular, within uncertainties, to the orbit derived here, agreeing with the expectation that jets are launched perpendicular to their disks. Further evidence confirming the orbital orientation of this system comes from the comparison of our results with the spectropolarimetric results of Hoffman et al. (1998). They predict that the jets should be oriented along p.a.  $\sim 163.5^\circ$ , similar to that found by Umana et al. (2000) and roughly perpendicular to the orbital orientation we found.

Finally, we compare our measurements of the displacement between the  $H\alpha$  and continuum photocenters to predictions based on parameters of the system derived by others (e.g., Harmanec et al. 1996; Harmanec 2002; Linnell 2000). We use the reference system of Harmanec et al. (1996), where the orbit is in the  $X - Y$  plane, with the origin at the most massive star (the one that is currently gaining mass) and the  $X$ -axis

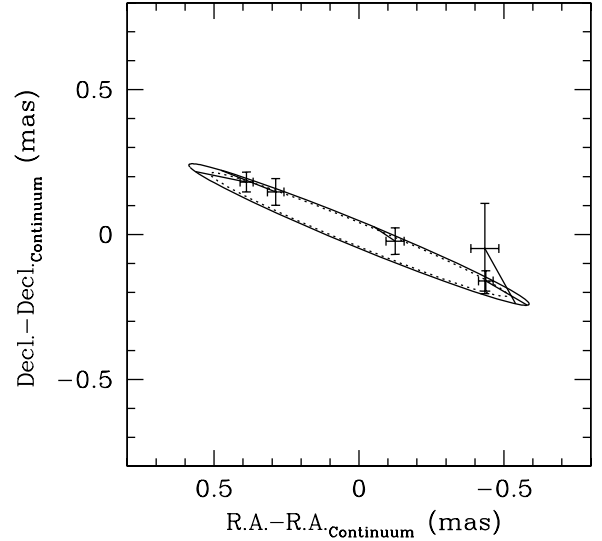


**Figure 10.**  $H\alpha$  emission positions compared to model orbits. The solid line shows the model orbit based on the parameters discussed in Section 5. The dotted line shows the same orbit, but with an assumed distance of 309 pc,  $1\sigma$  greater than the *Hipparcos* distance. The lines connecting the emission positions to the orbit indicate the model position along the orbit for each night.

defined by the line joining the two stars. The analysis of the radial velocities of this system shows that the eccentricity of the orbit is 0 (Harmanec & Scholz 1993). According to Harmanec (2002), the separation between the centers of the two stars is  $58.52 R_\odot$ . For  $\Delta m = 0.9$  mag the position of the photocenter is at  $X = 40.64 R_\odot$  and  $Y = 0$ . Based on the analysis of the velocity curve of the  $H\alpha$  emission, Harmanec et al. (1996) found that this emission line originates in the disk at  $X = 4.12 R_\odot$ ,  $Y = 4.97 R_\odot$ , a region offset from the center of the system, possibly related to the point of impact of the gas in the disk.

We used these parameters to calculate the model orbits of the  $H\alpha$  and continuum photocenters, and converted them to positions in the sky using the inclination derived by Linnell et al. (1998;  $i = 86^\circ$ ), the orientation derived by us ( $\Omega_{H\alpha} = 249^\circ$ ), and a distance of 270 pc. The resulting  $H\alpha$  orbit relative to the continuum photocenter is shown in Figure 10 as a solid line.

The  $H\alpha$  orbit, at  $a_{H\alpha} = 0.46 \pm 0.01$  mas, is smaller than the model  $H\alpha$  orbit ( $a_{\text{model}} = 0.63$  mas) by 26%. There are several possible explanations. First, the system may be more distant than 270 pc. Increasing the distance by 39 pc ( $1\sigma$ ) would reduce the model orbit size by 14%. This suggestion is supported by a recent new reduction of the *Hipparcos* data (van Leeuwen 2007), which finds a distance of  $315^{+15}_{-13}$  pc for  $\beta$  Lyrae. Second, the magnitude difference may be smaller than 0.9 mag; if  $\Delta m = 0.8$  mag, the photocenter is closer to star 1, hence closer to the  $H\alpha$  emission, and the  $H\alpha$  orbit is reduced by  $\sim 3\%$ . However, we will show in the next section that the magnitude difference between the stars is likely to be higher than 0.9 mag.

Finally, an important source of error in the size of the measured  $H\alpha$  orbit is the correction for the continuum contribution to the  $H\alpha$  channel. Factors that contribute to errors in this correction are the uncertainty in the width of the channel and in the EW of the  $H\alpha$  absorption component. In this paper, we used the Coté & Waters (1987) calibration to correct for the  $H\alpha$  absorption in the stellar spectrum to obtain  $c_{\text{cnt}} = 0.87 \pm 0.01$  as the fractional contribution from the stellar photosphere to the flux in the  $H\alpha$  channel. However, their calibration is based on main-sequence stars and may overestimate the correction for  $\beta$  Lyrae, where the brightest component is a B6–8II star. We

**Table 2**  
Displacement of the H $\alpha$  and Continuum Photocenters

UT Date	Orbital Phase	$c_{\text{cnt}} = 0.87$		$c_{\text{cnt}} = 0.91$	
		R.A.(H $\alpha$ -Continuum) (mas)	Decl.(H $\alpha$ -Continuum) (mas)	R.A.(H $\alpha$ -Continuum) (mas)	Decl.(H $\alpha$ -Continuum) (mas)
2005 May 9	0.47	$-0.13 \pm 0.03$	$-0.02 \pm 0.05$	$-0.33 \pm 0.04$	$-0.13 \pm 0.07$
2005 May 18	0.17	$-0.44 \pm 0.05$	$-0.05 \pm 0.16$	$-0.75 \pm 0.04$	$-0.06 \pm 0.20$
2005 May 19	0.24	$-0.44 \pm 0.03$	$-0.16 \pm 0.04$	$-0.76 \pm 0.03$	$-0.25 \pm 0.05$
2005 May 24	0.63	$0.29 \pm 0.03$	$0.15 \pm 0.05$	$0.52 \pm 0.04$	$0.32 \pm 0.07$
2005 May 26	0.78	$0.39 \pm 0.02$	$0.18 \pm 0.03$	$0.73 \pm 0.04$	$0.33 \pm 0.06$

**Notes.** Columns 3 and 4 show the measurements obtained from images created using  $c_{\text{cnt}} = 0.87$ , while Columns 5 and 6 show the measurements from images created using  $c_{\text{cnt}} = 0.91$ . The orbital phases were calculated based on primary eclipse ephemerides from Kreiner (2004).

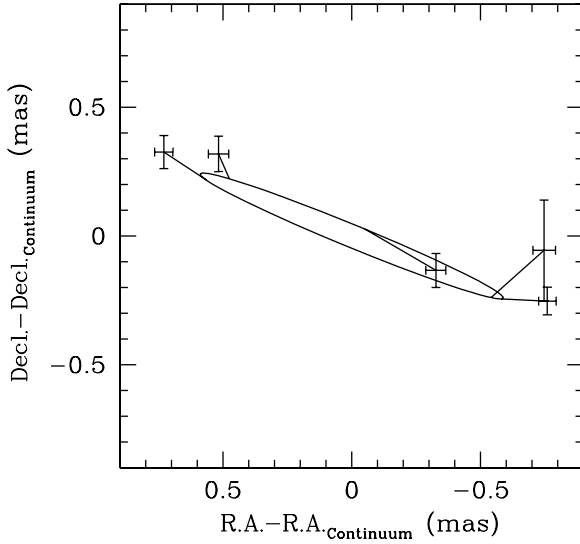


**Figure 11.** H $\alpha$  emission positions derived using a larger correction for the continuum contribution to the H $\alpha$  channel ( $c_{\text{cnt}} = 0.91$ ). The solid line shows the model orbit for a distance of 270 pc.

tested the dependence of the orbit size on this correction by using the extreme assumption that the EW correction for the underlying absorption to H $\alpha$  is 0, which gives  $c_{\text{cnt}} = 0.91$ . Using this value, we obtained new images and remeasured the H $\alpha$  emission positions with respect to the continuum photocenter (Table 2). The result was to increase the separations by a factor of  $\sim 1.8$ , which increases  $a_{\text{H}\alpha}$  to  $\sim 0.85$  mas, or  $\sim 30\%$  larger than  $a_{\text{model}}$  (Figure 11). We can infer that even a  $1\sigma$  increase in  $c_{\text{cnt}}$  would increase  $a_{\text{H}\alpha}$  to  $\sim 0.545$  mas.

## 6. COMPARISON BETWEEN DIFFERENTIAL PHASE AND $V^2$ RESULTS

As a way to check the H $\alpha$  orbit obtained with the differential phase technique, we use the calibrated continuum  $V^2$  and closure phases to determine the separation  $\rho$ , position angle  $\theta$ , and magnitude difference of the binary for each night. The Harmanec et al. (1996) model of the locations of the stellar components and the H $\alpha$  emission within the  $\beta$  Lyrae system then allow us to determine whether the binary and the H $\alpha$  orbits are consistent with one another.

To determine the binary orbit, we fit  $\rho$ ,  $\theta$ ,  $\Delta V$ , and  $\Delta R$  to each night's  $V^2$  and closure phase data. We did a grid search for the parameters that minimize  $\chi^2$ . The range of parameters used was  $0.5 < \rho < 2.0$  mas in steps of 0.01 mas,  $0^\circ < \theta < 360^\circ$  in

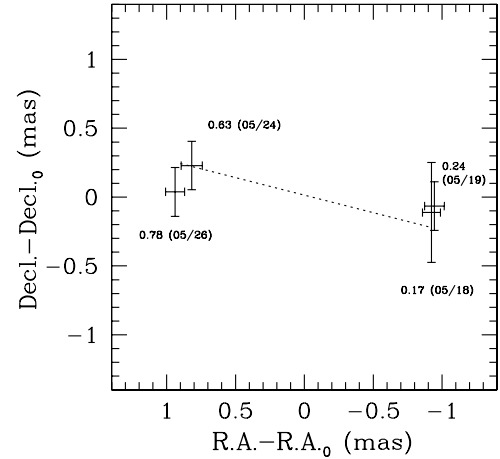


**Figure 12.** Separation of the two binary components, obtained by fitting the continuum  $V^2$  data. For each point we show the uncertainty in the position of the separation of the two sources. Beside each point we also indicate the orbital phase and the date of the observation. The dotted line was obtained by fitting a least squares line to the data, and approximates the orientation of the orbit in the plane of the sky ( $\Omega_{\text{bin}} = 256^\circ$ ).

steps of  $0^\circ 01$ ,  $0.7 < \Delta V < 1.9$  mag, and  $0.7 < \Delta R < 1.9$  mag in steps of 0.01 mag. We obtained the values given in Table 3 and plotted in Figure 12. Note that we could not converge on a fit for the night 2005 May 09, when a significant part of star 1 is hidden behind the donor star. The best-fit orbit to these points has  $a_{\text{bin}} = 0.99 \pm 0.03$  mas,  $\Omega_{\text{bin}} = 255^\circ \pm 7^\circ$ , and  $T_{\text{bin}} = \text{JD}2453493.47 \pm 0.34$ , where the subscript “bin” refers to the binary orbit, as distinct from the H $\alpha$  orbit. The orbital parameters obtained here as well as those obtained fitting the H $\alpha$  measurements are given in Table 4.

The value for  $a_{\text{bin}}$  is very close to the predicted value of 1.01 mas. The uncertainty in the orbital positions is large, in part because the baselines we used do not fully resolve this system, as can be seen in Figure 13. Here we present, for each night, the  $V^2$  of one scan taken with the longest baseline (AW0–E06, 53 m) within 30 minutes of meridian crossing, when the resolution for this baseline is highest. This figure shows some of the limitations of our measurements. As one would expect, we observe higher  $V^2$  on the night of May 24, when the system is close to eclipse, and lower  $V^2$  on May 19 and May 26, when the separation of the stars is close to its maximum. However, our baselines are not long enough to show the full characteristic cosine wave signature of a binary, which increases the uncertainty in the determination of the separation and magnitude difference of the two stars. Future work, using longer baselines, will be able to reduce the uncertainties in these values.

**Table 3**  
Binary Separations

UT Date	Orbital Phase	$\rho$ (mas)	$\theta$ (deg)	$\Delta_{\text{Maj}}$ (mas)	$\Delta_{\text{Min}}$ (mas)	$\phi$ (deg)	$\Delta V$ (mag)	$\Delta R$ (mag)
2005 May 18	0.17	0.93	263.1	1.09	0.19	177.9	$1.38 \pm 0.1$	$1.20 \pm 0.1$
2005 May 19	0.24	0.95	266.1	0.52	0.21	2.7	$1.23 \pm 0.1$	$1.20 \pm 0.1$
2005 May 24	0.63	0.85	74.4	0.51	0.23	3.8	$1.24 \pm 0.1$	$1.20 \pm 0.1$
2005 May 26	0.78	0.94	87.7	0.52	0.21	1.9	$1.34 \pm 0.1$	$1.18 \pm 0.1$

**Notes.** Column 1: date of the observations; Column 2: orbital phase; Columns 3 and 4: binary separation and position angle; Columns 5–7: position uncertainty ellipse major axis, minor axis, and position angle; Columns 8 and 9: magnitude difference between the two sources.

**Table 4**  
Orbital Elements

Data	Value
$a_{\text{H}\alpha}$ (mas) <sup>a</sup>	$0.46 \pm 0.03$
$a_{\text{H}\alpha}$ (mas) <sup>b</sup>	$0.80 \pm 0.03$
$a_{\text{bin}}$ (mas)	$0.99 \pm 0.03$
$i$ (deg) <sup>c</sup>	86
$\Omega_{\text{H}\alpha}$ (deg)	$249 \pm 4$
$\Omega_{\text{bin}}$ (deg)	$255 \pm 7$
$e$ <sup>d</sup>	0
$\omega$ (deg)	270
$T_{\text{H}\alpha}$ (JD)	$2453493.77 \pm 0.23$
$T_{\text{bin}}$ (JD)	$2453493.47 \pm 0.34$
$P$ (days) <sup>e</sup>	12.9421

**Notes.**  $T_{\text{H}\alpha}$  and  $T_{\text{bin}}$  correspond to the fitted time of periastron passage just preceding our observations.

<sup>a</sup> Value obtained from images created assuming  $c_{\text{cnt}} = 0.87$ .

<sup>b</sup> Value obtained from images created assuming  $c_{\text{cnt}} = 0.91$ .

<sup>c</sup> Data from Linnell et al. (1998).

<sup>d</sup> Data from Harmanec & Scholz (1993).

<sup>e</sup> Data from Kreiner (2004).

To compare the  $\text{H}\alpha$  orbit with the binary orbit, we start with the model discussed in Section 5: the two stars are separated by  $58.52 R_{\odot}$ ; the continuum photocenter is located  $43.96 R_{\odot}$  from the more massive star (star 1), calculated using the average  $\Delta R = 1.20$  mag from Table 3; and the  $\text{H}\alpha$  emission is  $39.84 R_{\odot}$  from the photocenter, close to star 1 but  $4.97 R_{\odot}$  off the star-to-star line (Harmanec et al. 1996). This model implies that the  $\text{H}\alpha$  orbit around the continuum photocenter should have a semimajor axis 68% as big as that of the binary orbit, and it should lag star 1 in the binary orbit by  $\sim 0.02$  in orbital phase, or 0.25 days.

In Section 5, we found that  $a_{\text{H}\alpha} = 0.46 \pm 0.03$  mas, considerably smaller than 68% of the observed  $a_{\text{bin}} = 0.99 \pm 0.12$  mas. However, as also discussed in Section 5, the formal 0.01 uncertainty in  $c_{\text{cnt}}$  corresponds to a  $\sim 0.085$  mas uncertainty in  $a_{\text{H}\alpha}$ , which is larger still if we take into account the further uncertainty of applying the Coté & Waters (1987) calibration to the luminosity class II primary of  $\beta$  Lyrae. Given the uncertainties,  $a_{\text{H}\alpha}$  and  $a_{\text{bin}}$  are not inconsistent.

The orientations of the orbits derived from the two methods are quite consistent. Our orbital fits give  $\Omega_{\text{H}\alpha} = 249^\circ \pm 4^\circ$  and  $\Omega_{\text{bin}} = 255^\circ \pm 7^\circ$ , which agree well within the uncertainties. The phase lag  $T_{\text{H}\alpha} - T_{\text{bin}}$  between our calculated time of periastron passage for the  $\text{H}\alpha$  and binary orbits,  $0.30 \pm 0.41$  days or  $0.023 \pm 0.032$  in orbital phase, is also in very good agreement with the model predictions.

Another important result obtained from the analysis presented here is the magnitude differences between the two stars. The

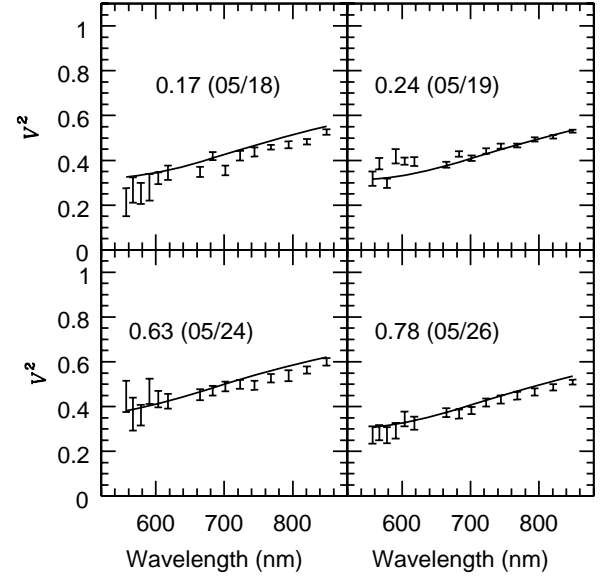


**Figure 13.** Calibrated  $V^2$  data from  $\beta$  Lyrae observed with the longest baseline, AW0–E06 (53 m). The respective nights and orbital phases are indicated inside the panels. In order to make the visualization of the plots easier each panel shows only one scan, corresponding to the one observed within 30 minutes of local meridian crossing. The solid lines show the best fitting model for the corresponding night.

value used in Section 5 ( $\Delta m = 0.9$  mag) was derived by Wilson (1974) using simple models. Based on a more detailed model, which fits the light curve at several bands simultaneously, Linnell et al. (1998) found  $\Delta V = 1.8$  mag at orbital phase 0.25. Our results show significantly smaller values,  $\Delta V = 1.30 \pm 0.1$  mag and  $\Delta R = 1.20 \pm 0.1$  mag, which will have important implications for the models of this binary system.

As a last check we used the method described by Tycner et al. (2005, 2006) to determine the size of the  $\text{H}\alpha$  disk. We used the calibrated  $\text{H}\alpha$   $V^2$ , corrected to eliminate the continuum contribution from the binary star to this channel. Following the results from Tycner et al. (2006) we decided to fit the  $\text{H}\alpha$   $V^2$  with a Gaussian model, which results in a disk with  $\text{HWHM} = 0.60 \pm 0.10$  mas (Figure 14). The Gaussian half width at half-maximum (HWHM) is comparable to the Roche lobe radius of  $\sim 0.52$  mas ( $30.3 R_{\odot}$  at 270 pc; Harmanec 2002), and consistent with the orbit obtained using the two methods described above.

## 7. SUMMARY

In this paper, we presented the development of a differential phase technique using NPOI data. We described the methods used to correct the instrumental and atmospheric effects on the phases of  $\beta$  Lyrae, which allowed us to recover the complex visibility of the  $\text{H}\alpha$  channel. We also described the procedure used to correct the continuum contribution to



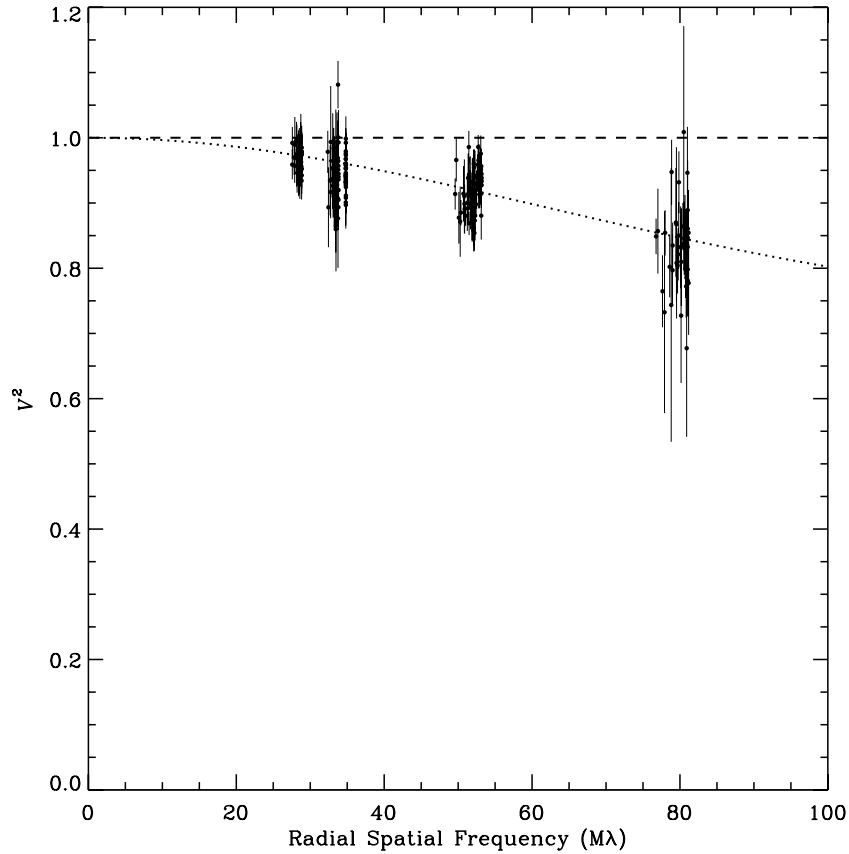


**Figure 14.** Calibrated  $V^2$  data for the  $H\alpha$  channel as a function of radial spatial frequency,  $(u^2 + v^2)^{1/2}$ . The dashed line shows the continuum  $V^2$  after the removal of the binary signature. The dotted line shows the best elliptical Gaussian model fitted to the data.

the  $H\alpha$  channel and successfully imaged the line emission of this system using standard radio interferometric techniques. We found that the major axis is oriented along  $\Omega = 249^\circ$ , consistent with previous spectropolarimetric measurements and, radio and optical interferometry results. From the comparison between the observed position of  $H\alpha$  relative to the continuum photocenter and values obtained from models, we find that our measurements indicate a semimajor axis for the  $H\alpha$  orbit that is smaller than that predicted by the models. We suggest that the most likely causes for this discrepancy are errors in the distance and in the correction for the continuum contribution to the  $H\alpha$  channel. We found that the results, obtained using the technique developed here, are consistent with those obtained from a more traditional analysis that uses only  $V^2$  and closure phase measurements. Also, based on the  $V^2$  analysis, we were able to determine the size of the  $H\alpha$  disk and the magnitude difference between the two stars, which is an important input to models of this system.

The technique presented here represents a major step in dealing with the problem of the loss of phase information in optical interferometric observations. At visual wavelengths, the phase fluctuations caused by atmospheric turbulence are both large and rapid, badly corrupting the measured fringe phases. Consequently, most optical interferometric imaging has been carried out using the square of the fringe amplitude,  $V^2$ , and the closure phase, in which the atmospheric phase fluctuations cancel. By making some assumptions about the structure of the source, our technique allows us to recover the fringe phase information, and thus to produce complex visibilities. With these complex visibilities in hand, we can

apply the image reconstruction techniques that are employed in radio interferometry.

In the case of  $\beta$  Lyrae, this technique allowed us to image the  $H\alpha$  emission and determine its location and motion with respect to the photocenter of the system, and thus to determine its orbit. We also found that the phases related to the  $He\ I$  emission have a behavior different from that of the  $H\alpha$ , suggesting that they are formed in different regions. As discussed in the introduction, there is evidence that the  $H\alpha$  emission of this system may originate in a jet (Harmanec et al. 1996; Hoffman et al. 1998; Umana et al. 2000). We do not see evidence for a jet in our images. However, this may be due to the lower resolution along the N–S direction, which is the direction along which the jet is expected to be oriented. Future observations with longer baselines will allow us to put better constraints on the existence and size of a jet.

Besides  $\beta$  Lyrae we are also applying this technique to other Be systems. This technique will allow us to image their circumstellar disks and map their structures, and study in better detail the accretion flow and effects such as the ionization of the disk by a binary companion.

The work done with the NPOI was performed through a collaboration between the Naval Research Lab and the US Naval Observatory, in association with Lowell Observatory, and was funded by the Office of Naval Research and the Oceanographer of the Navy. We thank the NPOI staff for the careful observations that contributed to this work. C.T. thanks Lowell Observatory for the generous time allocation on the John S. Hall 1.1 m telescope and thanks Wes Lockwood and Jeffrey Hall for supporting the Be star project on the Solar-Stellar Spectrograph. This research

has made use of the SIMBAD literature database, operated at CDS, Strasbourg, France. We acknowledge with thanks the variable star observations from the AAVSO International Database contributed by observers worldwide and used in this research. We thank Christian Hummel for the availability of the data reduction package OYSTER. We also thank the anonymous referee for suggestions that helped improve this paper.

*Facilities:* NPOI, USNO, Lowell.

## REFERENCES

- Akeson, R. L., Swain, M. R., & Colavita, M. M. 2000, *Proc. SPIE*, 4006, 321
- Armstrong, J. T., et al. 1998, *ApJ*, 496, 550
- Baldwin, J. E., et al. 1996, *A&A*, 306, L13
- Buscher, D. F. 1994, in *IAU Symp.* 158, *Very High Angular Resolution Imaging*, ed. J. G. Robertson & W. J. Tango (Dordrecht: Kluwer), 91
- Coté, J., & Waters, L. B. F. M. 1987, *A&A*, 176, 93
- Cotton, W., et al. 2008, *Proc. SPIE*, 7013, 70131N
- Dobias, J. J., & Plavec, M. J. 1985, *AJ*, 90, 773
- Goodricke, J., & Englefield, H. C. 1785, *Philos. Trans. Ser. I*, 75, 153
- Hall, J. C., Fulton, E. E., Huenemoerder, D. P., Welty, A. D., & Neff, J. E. 1994, *PASP*, 106, 315
- Harmanec, P. 2002, *Astron. Nachr.*, 323, 87
- Harmanec, P., et al. 1996, *A&A*, 312, 879
- Harmanec, P., & Scholz, G. 1993, *A&A*, 279, 131
- Hoffman, J. L., Nordsieck, K. H., & Fox, G. K. 1998, *AJ*, 115, 1576
- Hummel, C. A., Mozurkewich, D., Armstrong, J. T., Hajian, A. R., Elias, N. M., II, & Hutter, D. J. 1998, *AJ*, 116, 2536
- Hummel, C. A., Mozurkewich, D., Benson, J. A., & Wittkowski, M. 2003b, *Proc. SPIE*, 4838, 1107
- Hummel, C. A., et al. 2003a, *AJ*, 125, 2630
- Ireland, M. J., Monnier, J. D., & Thureau, N. 2006, *Proc. SPIE*, 6268, 62681T
- Jorgensen, A. M., et al. 2006, *Proc. SPIE*, 6268, 47
- Jorgensen, A. M., et al. 2007, *AJ*, 134, 1544
- Kreiner, J. M. 2004, *Acta Astron.*, 54, 207
- Lawson, P. R., et al. 2006, *Proc. SPIE*, 6268, 62681T
- Linnell, A. P. 2000, *MNRAS*, 319, 255
- Linnell, A. P., Hubeny, I., & Harmanec, P. 1998, *ApJ*, 509, 379
- Monnier, J. D. 2003, *Rep. Prog. Phys.*, 66, 789
- Monnier, J. D., et al. 2007, *Science*, 317, 342
- Mourard, D., et al. 1992, in *ASP Conf. Ser.* 32, *IAU Colloq. 135: Complementary Approaches to Double and Multiple Star Research* (San Francisco, CA: ASP), 510
- Owens, J. C. 1967, *Appl. Opt.*, 6, 51
- Perryman, M. A. C., et al. 1997, *A&A*, 323, L49
- Peterson, D. M., et al. 2006a, *ApJ*, 636, 1087
- Peterson, D. M., et al. 2006b, *Nature*, 440, 896
- Quirrenbach, A. 2000, in *Principles of Long Baseline Stellar Interferometry*, ed. P. R. Lawson (Pasadena, CA: NASA/JPL), 143
- Quirrenbach, A., Buscher, D. F., Mozurkewich, D., Hummel, C. A., & Armstrong, J. T. 1994, *A&A*, 283, L13
- Thiébaud, E. 2008, *Proc. SPIE*, 7013, 70131I
- Tycner, C., et al. 2005, *ApJ*, 624, 359
- Tycner, C., et al. 2006, *AJ*, 131, 2710
- Umana, G., Maxtel, P. F. L., Triglio, C., Fender, R. P., Leone, F., & Yerli, S. K. 2000, *A&A*, 358, 229
- Vakili, F., Mourard, D., Bonneau, D., Mourand, F., & Stee, P. 1997, *A&A*, 323, 183
- Vakili, F., et al. 1998, *A&A*, 335, 261
- van Leeuwen, F. H. 2007, in *The New Reduction of the Raw Data, ASSL*, (Dordrecht: Springer), 350
- van Moorsel, G., Kenball, A., & Greisen, E. 1996, in *ASP Conf. Ser.* 101, *Astronomical Data Analysis Software and Systems V*, ed. G. H. Jacoby & J. Barnes (San Francisco, CA: ASP), 37
- Wilson, R. E. 1974, *ApJ*, 189, 319
- Yoon, J., et al. 2007, *PASP*, 119, 437